Journal of Zhejiang University-SCIENCE A (Applied Physics & Engineering) *2025 26(7):694-706*
www.jzus.zju.edu.cn; www.springer.com/journal/11582
E-mail: jzus_a@zju.edu.cn

Research Article

https://doi.org/10.1631/jzus.A2400308

Effect of mesoporous FA-SiO_2 extracted from fly ash on the structural and photocatalytic properties of g-C_3N_4-based materials

Xianhua LI[1,2], Qingbo YU[1,3]✉

[1]*The First Affiliated Hospital of Anhui University of Science and Technology (Huainan First People's Hospital), Huainan 232001, China*
[2]*School of Mechatronic Engineering, Anhui University of Science & Technology, Huainan 232001, China*
[3]*School of Materials Science and Engineering, Anhui University of Science & Technology, Huainan 232001, China*

Abstract: To explore high value-added utilization pathways of fly ash, the mesoporous structure of silicon dioxide extracted from fly ash (FA-SiO_2) was utilized to restrict the dicyandiamide (DCDA) thermal degradation process. This produced chemically bonded interacting composite photocatalysts of FA-SiO_2 and graphitic-phase carbon nitride (g-C_3N_4). Compared with the spherical silicon dioxide prepared using tetraethyl orthosilicate (TEOS-SiO_2), the mesoporous structure of FA-SiO_2 allowed DCDA to react in a smaller space, which facilitated the transformation of DCDA to melamine by the thermal degradation kinetics of FA-SiO_2/DCDA. This ultimately boosted the formation of an N-atom-removed triazine ring structure and a multistage structure combining lumps and rods in the composite photocatalysts of g-C_3N_4 and FA-SiO_2, which led to a higher visible-light utilization efficiency, a suitable valence-band position, and the photocatalytic activity for methylene blue reaching 3.56 times that of g-C_3N_4. The findings indicate that mesoporous FA-SiO_2 has the potential to improve the structural and photocatalytic properties of g-C_3N_4-based materials.

Key words: Fly ash (FA); FA-SiO_2; g-C_3N_4-based materials; Structural and photocatalytic properties

1 Introduction

Photocatalysis is regarded as a green technology for the treatment of pollutants such as dyes and antibiotics, and is crucial for improving the current growing environmental pollution problem (Weng et al., 2018; Momin et al., 2024a). Graphitic phase carbon nitride (g-C_3N_4) has attracted extensive research due to a series of excellent properties such as low cost, easy preparation, chemical stability, and a moderate band gap (Niu et al., 2018; Wang et al., 2018). g-C_3N_4 is usually prepared by thermal polymerization with nitrogen-rich materials such as dicyandiamide, melamine, or urea (Kumar et al., 2023), which results in the g-C_3N_4 exhibiting serious agglomeration, low specific surface area, and fewer surface active sites, as well as easy complexation of photogenerated electron–hole pairs (Momin et al., 2024b). These drawbacks inhibit the photocatalytic performance of g-C_3N_4 (Yan et al., 2009; Lan et al., 2016).

Various adjusted structures have been used to improve the photocatalytic performance of g-C_3N_4, such as elemental doping, construction of heterojunction structures and defect engineering (Chen et al., 2022; Yang et al., 2022; Wang N et al., 2023; Yu et al., 2023). Regulating the condensation process of precursors toward g-C_3N_4 can effectively control its structure, thereby influencing its photocatalytic performance (He et al., 2024). Yu et al. (2023) obtained g-C_3N_4 with a porous structure, high specific surface area, more amino functional groups, and a more stable chemical bonding structure by controlling the synthesis temperature of precursors. Yuan et al. (2015) also synthesized g-C_3N_4 with different chemical structures by controlling the polymerization temperature. Instead of changing the synthesis temperature, Wan et al. (2018) controlled the polymerization of g-C_3N_4 by means of the limiting effect of the pores in Y-type zeolite. The result was g-C_3N_4 with a controlled degree of polymerization, which exhibited different photoluminescence properties

✉ Qingbo YU, yuqingbo007@163.com
Xianhua LI, https://orcid.org/0000-0002-0524-2469

Received June 17, 2024; Revision accepted Sept. 6, 2024;
Crosschecked May 19, 2025; Online first June 27, 2025

due to the confining effect of sub-nanometer-sized cages in the molecular sieves (Wan et al., 2018).

Regulating by means of mesoporous structure materials is a feasible concept for the polymerization process of g-C_3N_4. At this stage of exploration, a variety of mesoporous materials have been used to regulate the polymerization process of g-C_3N_4, such as zeolite molecular sieves, metal-organic frameworks (MOFs), clays, and mesoporous SiO_2 (Zhao et al., 2018; Chen et al., 2020; Khan et al., 2023; Nair et al., 2024). Compared to other substrates, mesoporous SiO_2 offers ultraviolet–visible transparency and chemical stability. It has been shown that g-C_3N_4 prepared with mesoporous SiO_2 modulation exhibits excellent photocatalytic activity, which is attributable to its intrinsic structure and the quantum confinement effect (Wang et al., 2019).

Fly ash (FA) is a solid waste discharged from thermal power generation which has a large storage capacity, is difficult to handle, and causes extensive pollution to the ecological environment. Thus, finding a way to comprehensively utilize it is an attractive topic for research. For example, FA can be embedded in MnO_2 for more effective mineralization of bisphenol-A and adsorption of Congo red (Angaru et al., 2024). In addition, the main components of FA are SiO_2 and Al_2O_3, which are effective resources for the preparation of SiO_2, $Al(OH)_3$, and Al_2O_3. However, the porous SiO_2 extracted from FA is rarely used to regulate the structure and properties of g-C_3N_4, especially analyzed the reason for regulation by thorough thermodynamic analysis.

In this work, mesoporous SiO_2 was derived from FA and employed to modulate the formation of g-C_3N_4. The structural and photocatalytic properties of the resulting materials (FA-SiO_2/g-C_3N_4) were systematically analyzed using Fourier-transform infrared spectroscopy (FTIR), X-ray diffraction (XRD), scanning electron microscope (SEM), and X-ray photoelectron spectroscopy (XPS) techniques. We also looked at the effects of different SiO_2 structures on the polymerization process of g-C_3N_4 during thermal decomposition by non-isothermal kinetic analysis.

2 Experimental section

2.1 Materials

The chemical reagents used in the experiment were all of analytical grade. The tetraethyl orthosilicate (TEOS, 98.0%), sodium carbonate (99.5%), and dicyandiamide (99.0%) were produced by Shanghai Aladdin Biochemical Technology Co., Ltd., China. The FA was produced by Huainan Mining (Group) Co., Ltd., China.

2.2 Preparation of silicon dioxide

Mesoporous silicon dioxide derived from FA (Fig. S1 of the electronic supplementary materials (ESM)): a mixture of sodium carbonate (10 g) and FA (10 g) was subjected to thermal treatment by heating at a rate of 10 ℃/min to 850 ℃ and maintained at that temperature for 2 h. Subsequently, 5 g of the obtained materials was dispersed in 40 mL of 3 mol/L HCl and stirred for 30 min. The suspension was then centrifuged, and the resulting mixture was transferred to a sealed reactor and held at 100 ℃ for 24 h. The colloid was obtained and washed to neutral. Finally, it was freeze-dried to produce the powdered material, which was recorded as FA-SiO_2.

Silicon dioxide prepared from TEOS: ethanol (50 mL), ammonia (10 mL, 25%), and deionized water of 20 mL were mixed at 35 ℃. The TEOS (5 mL) was added and stirred for 2 h. After centrifugation, the powder was washed with ethanol and dried at 60 ℃ to obtain the white powder, which was recorded as TEOS-SiO_2.

2.3 Preparation of silicon dioxide and dicyandiamide composite precursor

Dicyandiamide (DCDA, 2.5 g) was added to 25 mL of deionized water and stirred to dissolve at 70 ℃. Silicon dioxide (0.5 g) was added, then stirred for 2 h. The obtained mixed liquid was placed in a room-temperature environment until crystallization occurred, and then filtered and dried to produce the precursor. The precursor obtained by crystallization of TEOS-SiO_2 and dicyandiamide was recorded as TEOS-SiO_2/DCDA, and the precursor obtained by crystallization of FA-SiO_2 and dicyandiamide was recorded as FA-SiO_2/DCDA.

2.4 Preparation of g-C_3N_4-based composite photocatalysts

The above-described precursors TEOS-SiO_2/DCDA and FA-SiO_2/DCDA were heated to 550 ℃ in N_2 atmosphere at a heating rate of 2.5 ℃/min and held for 4 h. The precursors were naturally cooled to room temperature and preserved by milling, and the resulting substances were recorded as TEOS-SiO_2/g-C_3N_4 and FA-SiO_2/g-C_3N_4, respectively.

3 Results and discussion

3.1 Structural study of silicon dioxide

Figs. S2 and S3 show the FTIR, XRD, and SEM spectra of silicon dioxide. It can be seen that the peak intensity and position of FA-SiO_2 remain basically the same compared to TEOS-SiO_2, implying successful extraction of FA-SiO_2 from FA (Du et al., 2018; Han et al., 2019; Liu et al., 2019; Kantor et al., 2022). The FA-SiO_2 exhibits a blocky structure made up of a combination of fine particles, which is different from the spherical shape of TEOS-SiO_2 (Fig. S3). As shown in Fig. 1, the specific surface area of FA-SiO_2 is 703.02 m^2/g, the average pore size is 4.99 nm, and the pore volume is 0.8135 cm^3/g, which is obtained by calculating the area under the integral curve. Unlike nonporous TEOS-SiO_2, the pore structure of FA-SiO_2 may limit the polymerization reaction of DCDA when used in FA-SiO_2/DCDA.

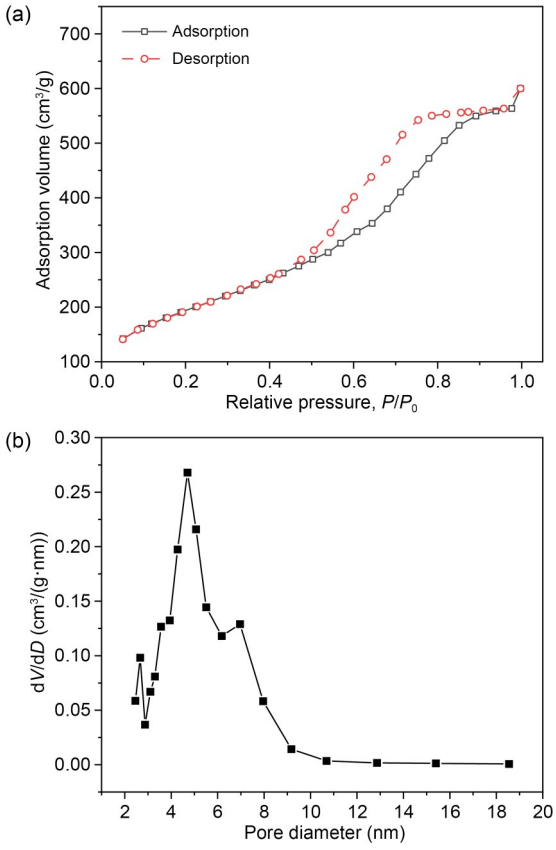

Fig. 1 (a) N_2 adsorption–desorption isotherm of FA-SiO_2; (b) aperture distribution curve. P and P_0 are the equilibrium pressure and saturation pressure of the adsorbate gas, respectively; dV and dD are the differential pore volume and differential pore diameter, respectively

3.2 Structural study of the composite precursors of silicon dioxide and dicyandiamide

The structure of a precursor can affect the structure of the photocatalyst and subsequently catalytic performance, so it was important to investigate this aspect. Fig. 2a shows the FTIR spectra of DCDA, TEOS-SiO_2/DCDA, and FA-SiO_2/DCDA. It is evident that TEOS-SiO_2/DCDA and FA-SiO_2/DCDA have similar infrared absorption spectra to DCDA, indicating that the basic structure of DCDA was preserved. TEOS-SiO_2/DCDA and FA-SiO_2/DCDA have new absorption peaks at 1090 cm^{-1} and 1074 cm^{-1}, respectively, which we attribute to the asymmetric stretching vibrational peak of Si–O–Si. This suggests the presence of a complex between SiO_2 and DCDA in the precursor. It is noteworthy that the absorption peak in TEOS-SiO_2/DCDA at 1090 cm^{-1} is significantly stronger than that of FA-SiO_2/DCDA at 1074 cm^{-1}, which could be attributed to the fact that DCDA is encapsulated on the surface of FA-SiO_2 during the

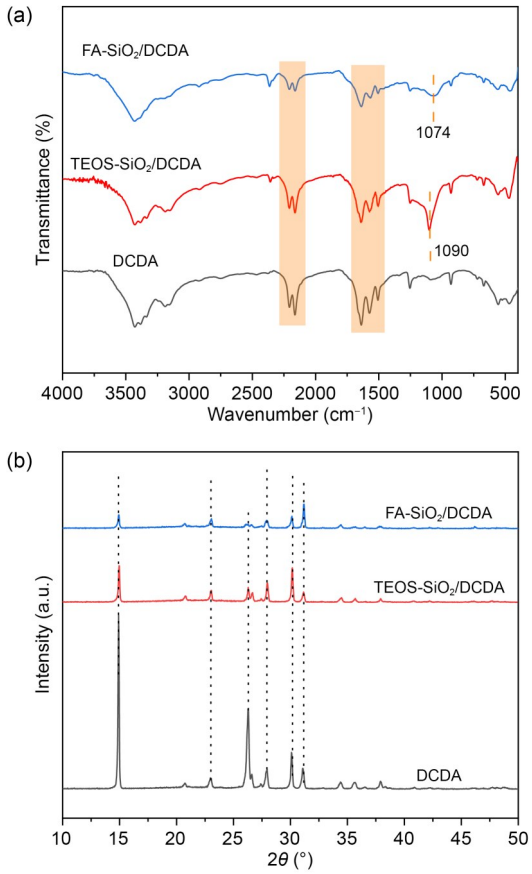

Fig. 2 (a) FTIR spectra and (b) XRD spectra of DCDA, TEOS-SiO_2/DCDA, and FA-SiO_2/DCDA

crystallization process, making the vibrational peak of Si–O–Si difficult to discern. In addition, the peak of Si–O–Si in FA-SiO_2/DCDA appears at 1074 cm^{-1}, while the peak of Si–O–Si in FA-SiO_2 appears at 1091 cm^{-1} (Fig. S2a), which is slightly blue-shifted compared to FA-SiO_2. The peak position of Si–O–Si in TEOS-SiO_2/DCDA remains basically the same as that of TEOS-SiO_2 (Fig. S2a). This may be due to the fact that FA-SiO_2 has a high specific surface area and pore volume, which causes interaction between DCDA and the skeleton structure of FA-SiO_2 during the crystallization process. Subsequently, internal stress is generated in the skeleton structure of FA-SiO_2, leading to a change in the atomic arrangement between DCDA and FA-SiO_2, and consequently to a change in the lattice constants of the complex, resulting in a slight blue shift in the peak position of Si–O–Si in FA-SiO_2/DCDA (Jia et al., 2023).

We examined the crystal structure of the precursor with XRD. As can be seen in Fig. 2b, the diffraction peaks of DCDA appear in both TEOS-SiO_2/DCDA and FA-SiO_2/DCDA, and the peak positions of the diffraction peaks are basically the same as that of DCDA, but there is a change in the intensity of the peaks. This suggests that the presence of SiO_2 affects the crystallinity of DCDA, and that TEOS-SiO_2 and FA-SiO_2 change the priority of surface crystal growth of DCDA in the process of recrystallization.

Fig. 3 shows the SEM images of DCDA, TEOS-SiO_2/DCDA, and FA-SiO_2/DCDA. As shown in Fig. 3a, DCDA exhibits blocky aggregation. The microstructure of DCDA changed after it was compounded with TEOS-SiO_2 and FA-SiO_2. As shown in Fig. 3b, TEOS-SiO_2 particles with uniform particle size are stacked together, and DCDA fills in the pore structure formed by this particle stacking. Aggregation of fine particles was observed in FA-SiO_2/DCDA (Fig. 3c), which is consistent with the results shown in Fig. 3b, where the particles have infiltrated DCDA, indicating that an effective composite of FA-SiO_2 and DCDA has formed.

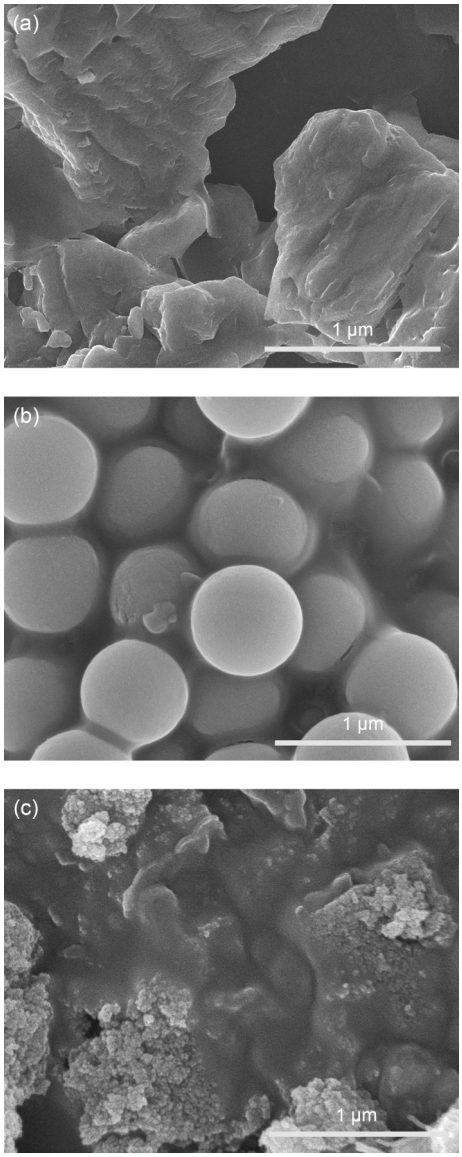

Fig. 3 SEM images of (a) DCDA, (b) TEOS-SiO_2/DCDA, and (c) FA-SiO_2/DCDA

3.3 Structural study of composite photocatalysts

Fig. 4a shows the FTIR spectra of g-C_3N_4, TEOS-SiO_2/g-C_3N_4, and FA-SiO_2/g-C_3N_4. In the case of pure g-C_3N_4, the prominent absorption band near 808 cm^{-1} and the broad bands in the range of 1200–1700 cm^{-1} represent the main characteristic vibrations of the triazine ring structure and the conjugated C–N/C=N bonds within the g-C_3N_4 framework (Zhang et al., 2018; Meng et al., 2022). Compared to pristine g-C_3N_4, the vibrational peaks of TEOS-SiO_2/g-C_3N_4 and FA-SiO_2/g-C_3N_4 at 3100–3500 cm^{-1} are weak, indicating a decrease in the number of amines. The absorption peak of Si–O–Si in FA-SiO_2/g-C_3N_4 appeared at 1079 cm^{-1}, whereas the peak appeared at 1091 cm^{-1} for FA-SiO_2 (Fig. S2a) and was slightly blue-shifted. We attribute this to the interaction between FA-SiO_2 and g-C_3N_4 within the pore structure, which resulted in a change in the lattice constants of FA-SiO_2/g-C_3N_4 and led to the blue-shifted absorption peak of Si–O–Si, which was consistent with that of the precursor (Fig. 2a).

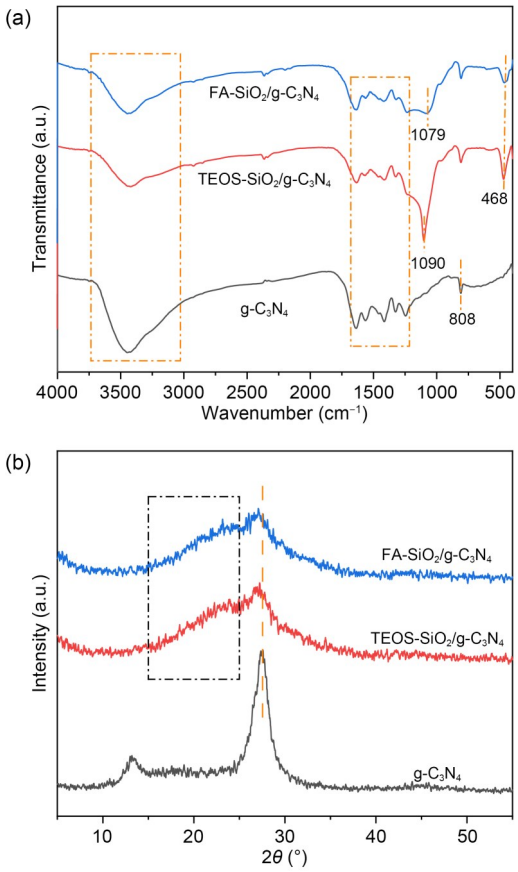

Fig. 4 (a) FTIR and (b) XRD spectra of g-C_3N_4, TEOS-SiO_2/g-C_3N_4, and FA-SiO_2/g-C_3N_4

The Si–O–Si absorption peak of TEOS-SiO_2/g-C_3N_4 appeared at 1090 cm^{-1}, and did not change significantly compared to the peak position of Si–O–Si in TEOS-SiO_2 (Fig. S2a). This could be attributed to the fact that the pore formed by the accumulation of TEOS-SiO_2 particles was too large to have a limiting effect on g-C_3N_4 polymerization. Compared with TEOS-SiO_2/g-C_3N_4, the absorption peaks of FA-SiO_2/g-C_3N_4 at 1079 cm^{-1} and 468 cm^{-1} were weakened, which may be due to the fact that FA-SiO_2 has a larger specific surface area and pore volume. g-C_3N_4 was encapsulated on the surface of FA-SiO_2, which was more completely complexed with g-C_3N_4, thus weakening the vibrational peaks of Si–O–Si.

We carried out XRD analysis on g-C_3N_4, TEOS-SiO_2/g-C_3N_4, and FA-SiO_2/g-C_3N_4 samples, and the corresponding patterns are presented in Fig. 4b. For pristine g-C_3N_4, two well-defined diffraction peaks are observed at 13.1° and 27.4°, which are attributed to the (100) and (002) crystal planes, respectively. For TEOS-SiO_2/g-C_3N_4 and FA-SiO_2/g-C_3N_4, the broad peaks from 15.0° to 25.0° and the characteristic diffraction peak at around 27° imply the existence of SiO_2 and g-C_3N_4 in the photocatalysts. It is worth noting that the characteristic peak at around 27° underwent a small leftward shift compared to pristine g-C_3N_4, indicating an improvement in the interlayer spacing of g-C_3N_4.

The surface chemical states of g-C_3N_4, TEOS-SiO_2/g-C_3N_4, and FA-SiO_2/g-C_3N_4 were analyzed by XPS. As shown in Fig. 5a, the elements C, N, and O were detected in g-C_3N_4, TEOS-SiO_2/g-C_3N_4, and FA-SiO_2/g-C_3N_4, while the element Si was also detected in TEOS-SiO_2/g-C_3N_4 and FA-SiO_2/g-C_3N_4 (the content of each element is shown in Table S1). The elemental contents of C and N in FA-SiO_2/g-C_3N_4 were higher than that in TEOS-SiO_2/g-C_3N_4, indicating that the content of g-C_3N_4 in FA-SiO_2/g-C_3N_4 was higher than that in TEOS-SiO_2/g-C_3N_4, which might be due to the facts that the specific surface area and pore volume of FA-SiO_2 were higher than those of TEOS-SiO_2, and that more DCDA was adsorbed within the pore structure during the preparation process, while the closed environment within the pores also favored the conversion of DCDA to g-C_3N_4.

Fig. 5b presents the high-resolution C 1s XPS spectra of the photocatalyst samples. In the case of pristine g-C_3N_4, the C 1s spectrum can be deconvoluted into three distinct peaks located at 284.8, 286.19, and 288.12 eV. These peaks are assigned to adventitious carbon species adsorbed on the catalyst surface, C–NH_x bonding, and sp^2-hybridized N–C=N bonding within the aromatic carbon-nitrogen heterocyclic framework, respectively. The quantitative proportions of these carbon-related chemical states are summarized in Table 1. The relative content of the N–C=N component exhibits a gradual increase from pure g-C_3N_4 to TEOS-SiO_2/g-C_3N_4 and further to FA-SiO_2/g-C_3N_4. This may be caused by the restricted reaction space of DCDA (Figs. 3b and 3c). When FA-SiO_2 has a mesoporous structure, the polymerization reaction of DCDA occurs in a smaller space, and the more localized space restricts the polymerization of DCDA into the more triazine ring structure of g-C_3N_4. As illustrated in Fig. 5c, the high-resolution N 1s XPS spectrum of g-C_3N_4 reveals three distinct binding energy peaks located at 398.61, 399.89, and 400.98 eV, assigned to sp^2-hybridized nitrogen atoms, tertiary nitrogen species (N–$(C)_3$), and amino functional groups (–NH or –NH_2). The relative contents of these nitrogen species, summarized in Table 1, provide insight into the bonding

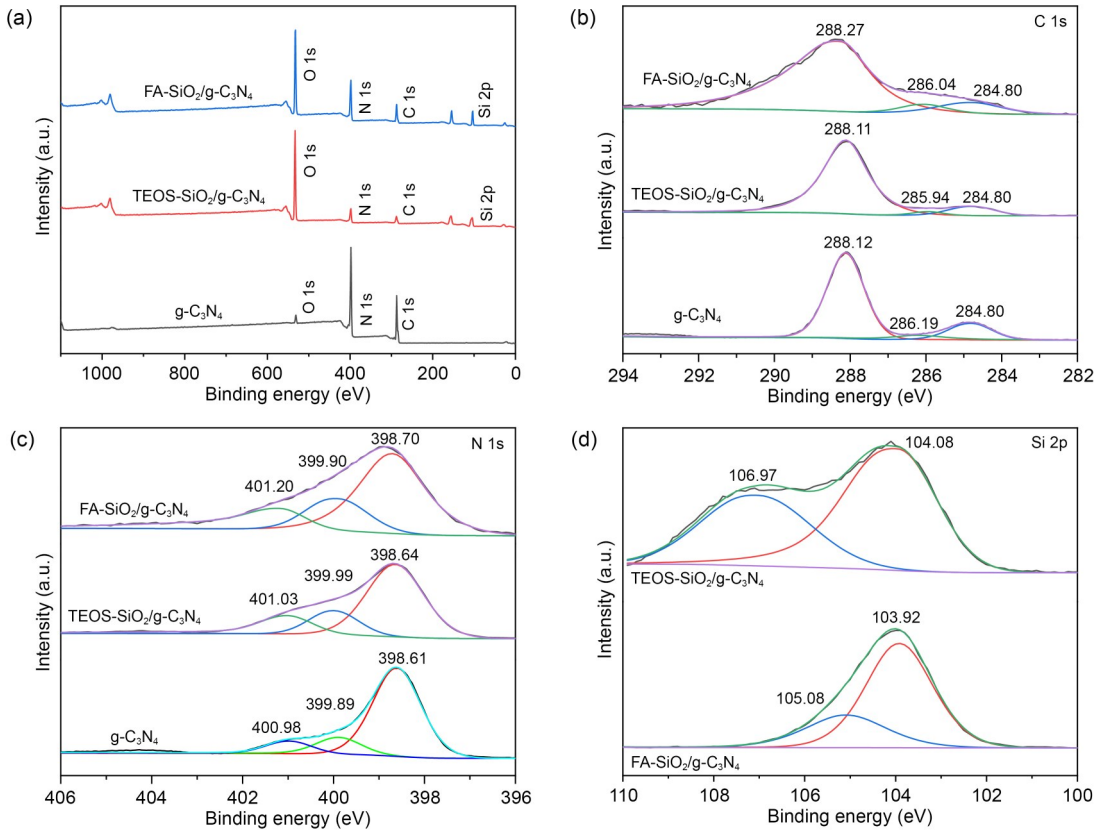

Fig. 5 (a) Full XPS spectrum; high-resolution XPS spectra of (b) C 1s, (c) N 1s, and (d) Si 2p pictures of g-C_3N_4, TEOS-SiO_2/g-C_3N_4, and FA-SiO_2/g-C_3N_4

Table 1 Proportions of chemical bonds containing C and N in g-C_3N_4, TEOS-SiO_2/g-C_3N_4, and FA-SiO_2/g-C_3N_4

Sample	Proportion of chemical bond (%)					
	C–C	C–NH_x	N–C=N	C=N–C	N–$(C)_3$	C–N–H
g-C_3N_4	15.94	7.05	77.01	71.98	15.65	12.37
TEOS-SiO_2/g-C_3N_4	10.66	6.71	82.63	58.13	20.43	21.44
FA-SiO_2/g-C_3N_4	10.44	2.14	87.42	64.31	17.27	18.42

environments and degree of condensation in the different photocatalyst samples. It is clear that the C=N–C content in TEOS-SiO_2/g-C_3N_4 and FA-SiO_2/g-C_3N_4 is reduced in comparison to that in g-C_3N_4, which may be due to the removal of N atoms from the CN framework structure. This would be in agreement with the FTIR analysis (Fig. 4a). The synthesis pathway of the SiO_2 and g-C_3N_4 composites is shown in Fig. S4. The Si 2p spectra are shown in Fig. 5d: the Si 2p peaks of SiO_2 in TEOS-SiO_2/g-C_3N_4 and FA-SiO_2/g-C_3N_4 appear at 104.08 eV and 103.92 eV, respectively. It is worth noting that a new Si 2p peak appears at 106.97 eV, which indicates that the chemical bonding between SiO_2 and g-C_3N_4 may have been established at the interface (Sun et al., 2021).

The microstructure and morphology of the three photocatalysts were investigated using SEM. The results showed that the microstructures of g-C_3N_4, TEOS-SiO_2/g-C_3N_4, and FA-SiO_2/g-C_3N_4 were very different. g-C_3N_4 had an obvious lamellar stacking structure (Fig. 6a). As seen in Fig. 6b, g-C_3N_4 filled in the pores formed by the stacking of TEOS-SiO_2 particles, consistent with the results observed in the precursor (Fig. 3b). A multistage structure combining lumps and rods was observed in FA-SiO_2/g-C_3N_4 (Fig. 6c). FA-SiO_2 has a large pore volume and mesoporous structure, which adsorbs DCDA during the preparation of the precursor. The DCDA adsorbed within the pores releases ammonia during the polymerization process, resulting in the extrusion of the g-C_3N_4 formed by

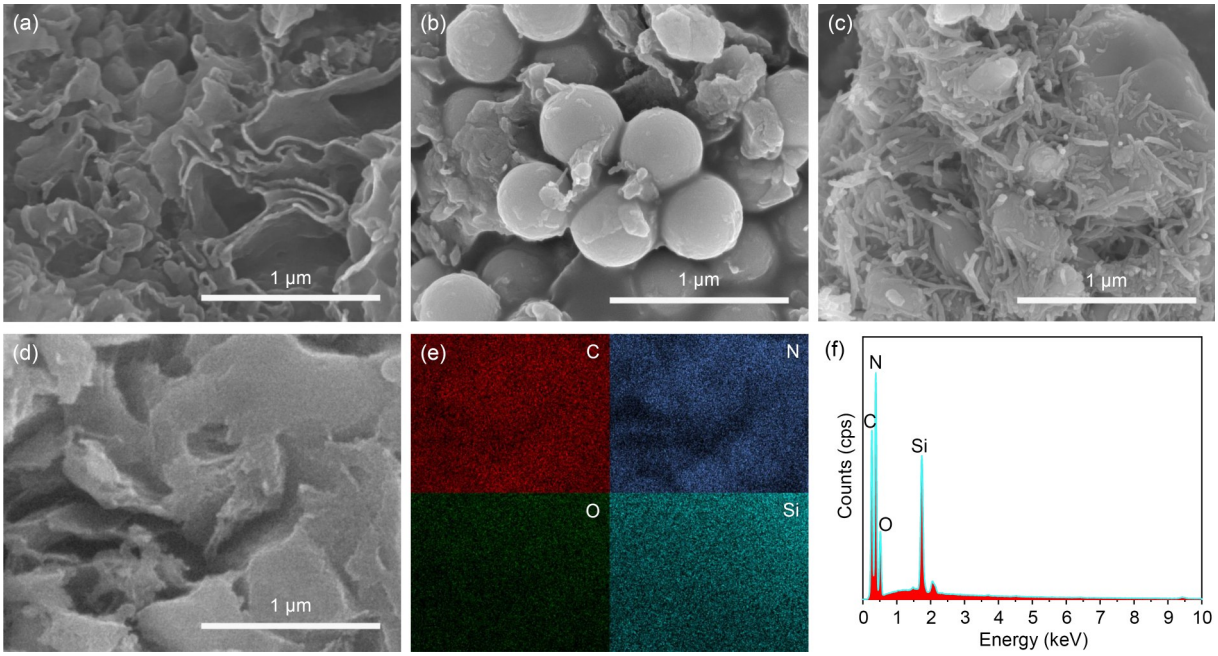

Fig. 6 SEM images of (a) g-C_3N_4, (b) TEOS-SiO_2/g-C_3N_4, and (c) FA-SiO_2/g-C_3N_4; (d) SEM image and (e) the corresponding elemental mapping; (f) EDS spectrum of FA-SiO_2/g-C_3N_4. References to color refer to the online version of this figure

polymerization within the pores. Thus, the unique nanoscale rod-like g-C_3N_4 structure is formed, which explains the blue shift of Si–O–Si absorption peaks. We observed this shift in the composite FA-SiO_2/g-C_3N_4 under infrared light when under the effect of stress. The nanorod-like structure of g-C_3N_4 in FA-SiO_2/g-C_3N_4 effectively increases its contact area with pollutants, which improves the photocatalytic activity. The elements in FA-SiO_2/g-C_3N_4 were detected using an energy dispersive spectrometer (EDS) (Fig. 6d), which showed that the samples contained the elements C, N, O, and Si. This matched the XPS detection results (Fig. 5a), further proving that an effective composite of FA-SiO_2 and g-C_3N_4 was formed.

3.4 Thermal decomposition kinetics study

We investigated the effect of precursor structure on the structure of the composite catalysts using thermal decomposition kinetic analysis. The DCDA, TEOS-SiO_2/DCDA, and FA-SiO_2/DCDA were tested by thermal analysis at heating rates of 5, 15, and 25 °C/min. The thermogravimetry (TG) and derivative thermogravimetry (DTG) curves of the three precursors were similar at different heating rates, indicating that the thermal decomposition processes of the three precursors were approximately the same, but there were differences in the temperature-related changes of the three precursors at various stages. From Figs. 7a and 7d, it is evident that the heating process of DCDA can be divided into five stages. In order to investigate the effect of the introduction of TEOS-SiO_2 and FA-SiO_2 on the polymerization process of DCDA in the precursors, we processed and analyzed the thermal decomposition kinetic data for the second stage of the three different precursors.

The activation energy E was determined by the Flynn-Wall-Ozawa method. Taking the conversion rate α as 0.1–0.9, we calculated the activation energy E of the three precursors. E represents the magnitude of the reaction resistance during the thermal condensation reaction of the precursors; the larger the resistance of the thermal condensation reaction, the larger the value of E. Compared with DCDA, E of the precursors TEOS-SiO_2/DCDA and FA-SiO_2/DCDA decreased (Fig. 8a), which could be attributed to the fact that the introduction of SiO_2 improves the aggregation of DCDA in the unit space, and makes the reaction easier to carry out, facilitating the formation of the triazine ring. This would be in accord with the XPS analysis. With the increase of conversion rate α, the activation energy of TEOS-SiO_2/DCDA gradually rose higher than that of FA-SiO_2/DCDA. This might be related to the mesoporous structure of FA-SiO_2, which restricts the reaction of dicyandiamide in FA-SiO_2/DCDA and forces it to take

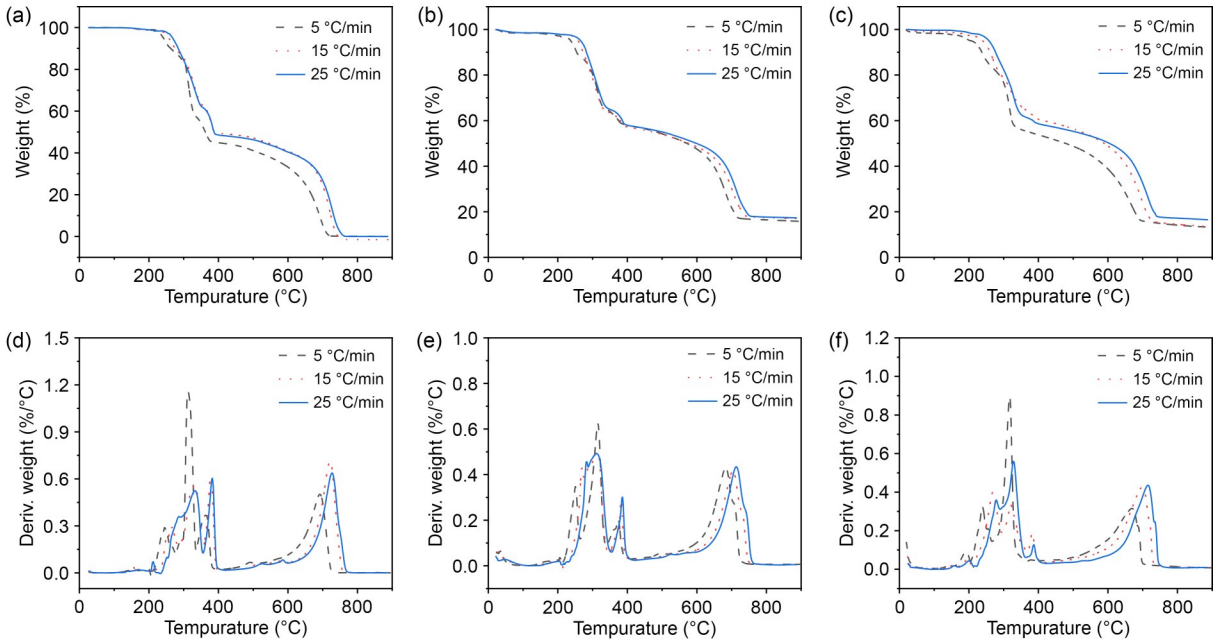

Fig. 7 TG curves of (a) DCDA, (b) TEOS-SiO_2/DCDA, and (c) FA-SiO_2/DCDA; DTG curves of (d) DCDA, (e) TEOS-SiO_2/DCDA, and (f) FA-SiO_2/DCDA

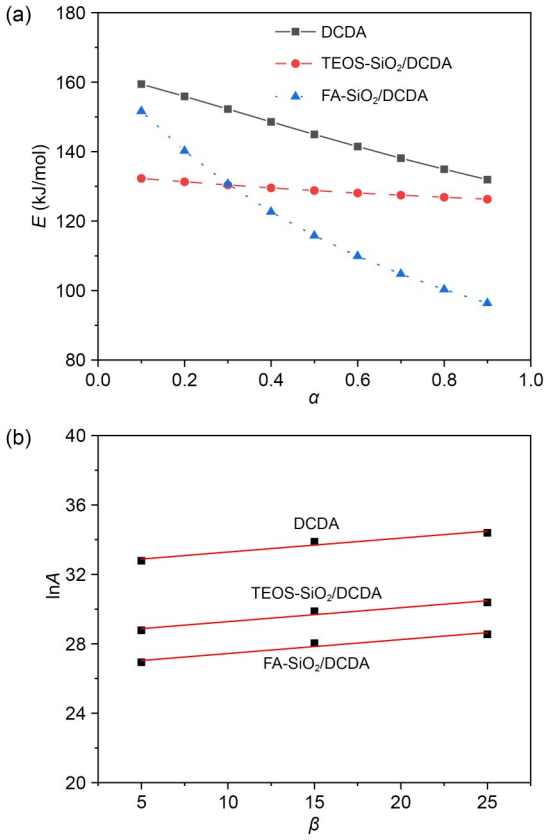

Fig. 8 (a) Relationship between conversion rate α and activation energy E; (b) relationship between pre-exponential factor A and heating rate β

place in a smaller space, fostering the conversion of dicyandiamide to melamine.

As shown in Fig. S5, $P(u)/P(0.5)$ values were obtained by substituting the activation energy E into the kinetic equation, where $P(u)$ is the temperature integral and $u=E/RT$, R is the gas constant and T is the temperature. The $P(u)/P(0.5)$-α plots were compared with standard $G(\alpha)/G(0.5)$-α curves to identify the reaction mechanism. DCDA matched the function $G(\alpha)=1-(2\alpha)/3-(1-\alpha)^{2/3}$ with a standard deviation of 0.26, while TEOS-SiO_2/DCDA and FA-SiO_2/DCDA followed $G(\alpha)=-\ln(1-\alpha)$, with deviations of 0.28 and 0.39, respectively.

The pre-exponential factor A was derived using the equations $Y=\ln(E/(\beta R))+\ln P(u)$ (β is the heating rate) and $X=\ln G(\alpha)$. By plotting Y against X and performing linear regression, the intercept yields $-\ln A$. Three different heating rates β were employed, resulting in corresponding A values for each material. As illustrated in Fig. 8b, A varies with β for all samples. The pre-exponential factor A reflects the frequency of atomic collisions, with higher values indicating more frequent and intense interactions. In this experiment, the descending order of A values for the three precursors is: DCDA, TEOS-SiO_2/DCDA, and FA-SiO_2/DCDA. The introduction of SiO_2 alters the aggregation of DCDA, resulting in a decrease in the collision probability, and

thus TEOS-SiO_2/DCDA and FA-SiO_2/DCDA have a lower pre-exponential factor *A* than that of DCDA. In addition, FA-SiO_2/DCDA has a lower finger prefactor *A* than DCDA. The mesoporous structure of FA-SiO_2 in FA-SiO_2/DCDA makes DCDA react in a smaller space, and the particles are limited by space. This reduces the collision probability, resulting in a lower *A*-value for FA-SiO_2/DCDA than TEOS-SiO_2/DCDA.

3.5 Photocatalytic performance study

The photocatalytic performance of the three photocatalysts was evaluated by measuring the degradation rate of methylene blue (MB) solution under simulated visible light. As shown in Fig. 9a, the degradation rate of g-C_3N_4 was 12.8% under continuous irradiation for 60 min, and the degradation rates of TEOS-SiO_2/g-C_3N_4 and FA-SiO_2/g-C_3N_4 under the same conditions were 18.9% and 37.3%, respectively. Their photocatalytic activity was 1.53 times and 3.56 times higher, respectively, than that of g-C_3N_4 (Fig. 9b). The enhanced photocatalytic performance of TEOS-SiO_2/g-C_3N_4 may be related to the removal of N atoms in the CN framework (Li et al., 2023). FA-SiO_2/g-C_3N_4 exhibited the best photocatalytic activity, which we attribute to the fact that not only was the chemical structure of FA-SiO_2/g-C_3N_4 improved, but also the mesoporous structure of FA-SiO_2. This caused the FA-SiO_2/g-C_3N_4 to form a more complex multilevel structure in terms of the microscopic morphology. The nanorod-like structure of g-C_3N_4 in FA-SiO_2/g-C_3N_4 can effectively increase the contact area with pollutants, which improves its photocatalytic activity. In addition, after five cycles of experiments, there was no significant change in the photocatalytic degradation efficiency (Fig. 9c).

To explore the photocatalytic remediation of methylene blue, we determined the high-performance liquid chromatography-mass spectrometry (LC-MS) of MB (Figs. S6 and S7). Characteristic peaks caused by the original MB molecules can be observed in Fig. S6a, and correspond to the peaks at *m*/*z* 284.01 and 285.33 in the mass spectrum (Fig. S6b) (Gnaser et al., 2005). Multiple new substance peaks were observed in the liquid chromatogram of MB after photocatalytic degradation (Fig. S7a), indicating the presence of multiple MB degradation intermediates in the solution after the catalytic degradation reaction. Except for the peak located at the retention time of 3.65 min, the other peaks

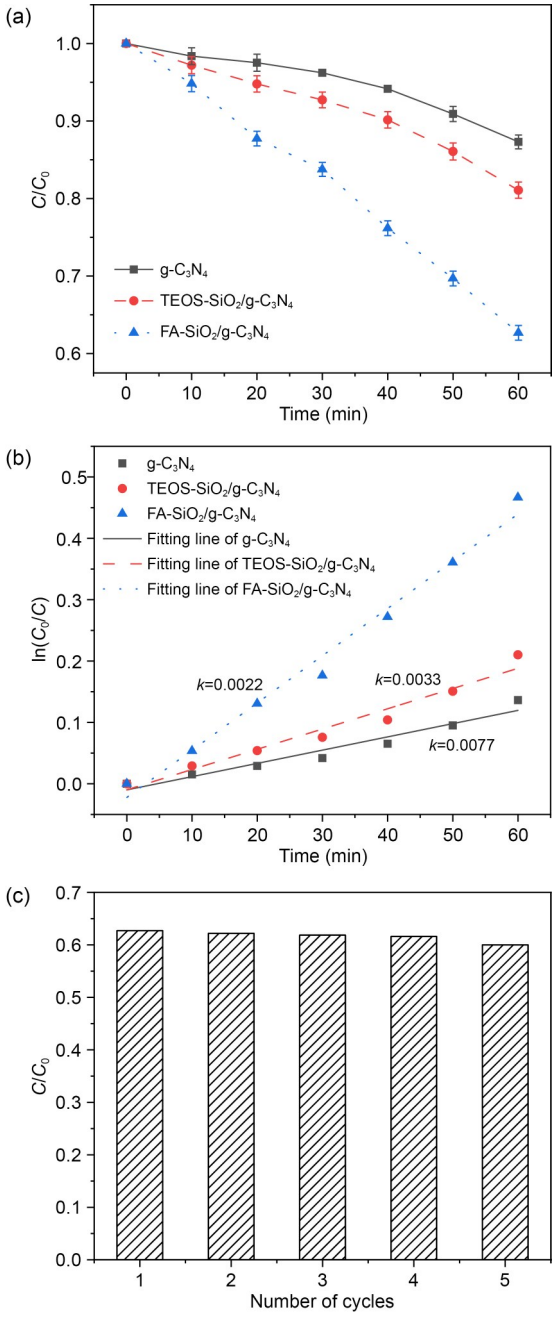

Fig. 9 (a) Photocatalytic degradation curve; (b) kinetic fitting lines of g-C_3N_4, TEOS-SiO_2/g-C_3N_4, and FA-SiO_2/g-C_3N_4; (c) photocatalytic cycle test of FA-SiO_2/g-C_3N_4. *C* and C_0 are the MB concentration varying with time and the initial concentration of MB, respectively. *k* represents the reaction rate constant

have small areas and low content, so further analysis was not necessary (Fig. S7b). Among them, the peak located at *m*/*z* 269.96 represents the intermediate product of the MB molecule losing one $-CH_3$, while the peak at *m*/*z* 256.93 originates from the intermediate

product of the MB molecule losing two –CH_3 (Bansode et al., 2017). Based on the above LC-MS results, it can be concluded that MB molecules are degraded in the form of dihydroxylation.

Next, we measured the optical properties of g-C_3N_4, TEOS-SiO_2/g-C_3N_4, and FA-SiO_2/g-C_3N_4 composites by ultraviolet–visible diffuse reflectance spectroscopy (DRS). As shown in Fig. 10a, g-C_3N_4, TEOS-SiO_2/g-C_3N_4, and FA-SiO_2/g-C_3N_4 all have significant absorption in the ultraviolet region. The ultraviolet–visible DRS of TEOS-SiO_2/g-C_3N_4 is slightly blue-shifted in comparison to the pristine g-C_3N_4, which suggests that the visible absorption becomes poorer, possibly due to the fact that the TEOS-SiO_2/g-C_3N_4 has a thinner stacked layer of g-C_3N_4 (Attri et al., 2023). FA-SiO_2/g-C_3N_4, on the other hand, exhibits a red shift towards longer wavelengths, indicating that FA-SiO_2/g-C_3N_4 has higher visible-light utilization compared to g-C_3N_4,

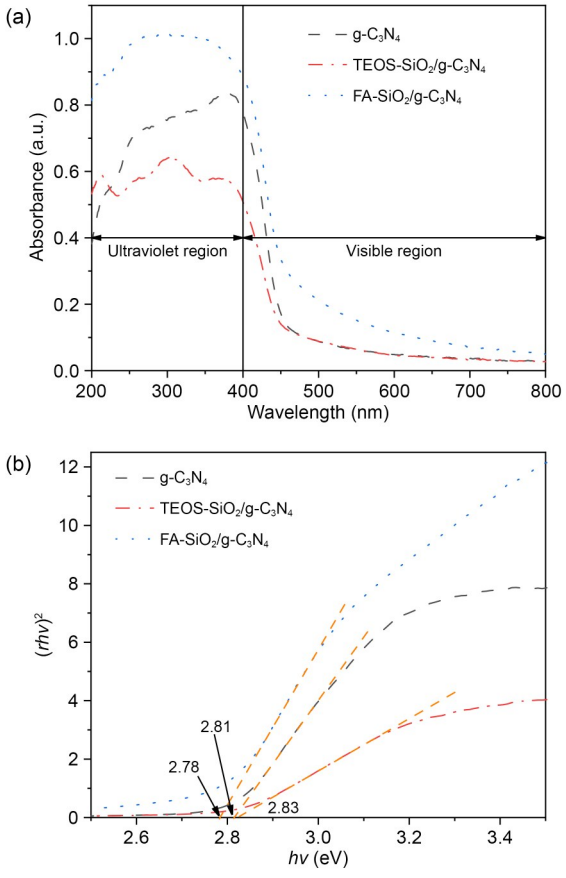

Fig. 10 (a) Ultraviolet–visible DRS and (b) relationship between $(rhv)^2$ and hv of g-C_3N_4, TEOS-SiO_2/g-C_3N_4, and FA-SiO_2/g-C_3N_4. The yellow dotted lines represent the tangent lines. References to color refer to the online version of this figure

which could be attributed to the better internal light reflection arising from the interlaced rod-like and layered multilevel structure (Wang TR et al., 2023). This may improve photocatalytic performance as well. From the equations $rhv=B(hv-E_g)^{1/2}$ and $E_g=1240/\lambda$ (r, h, v, E_g, B, and λ are the absorption coefficient, Planck's constant, optical frequency, bandgap energy, scaling factor, and wavelength, respectively), it can be calculated that the bandgap-energy values E_g of g-C_3N_4, TEOS-SiO_2/g-C_3N_4, and FA-SiO_2/g-C_3N_4 are 2.81, 2.83, and 2.78 eV, respectively (Fig. 10b).

As depicted in Figs. 11a–11c, the secondary cutoff edge potentials E_{cut} for g-C_3N_4, TEOS-SiO_2/g-C_3N_4, and FA-SiO_2/g-C_3N_4 were determined to be 17.38, 15.69, and 15.62 eV, respectively, while the corresponding Fermi edge potentials E_{FM} were 1.94, 0.42, and 0.48 eV. Based on the relation $E_{VBE}=hv-(E_{cut}-E_{FM})$ with hv= 21.22 eV, the calculated valence band edge potentials E_{VBE} were 5.78 eV for g-C_3N_4, 5.95 eV for TEOS-SiO_2/g-C_3N_4, and 6.08 eV for FA-SiO_2/g-C_3N_4. The E_{rhe} (reversible hydrogen electrode) at 0 V is equal to E_{vac} (vacuum energy level) at −4.44 eV. The valence band edge potentials E_{VB} of g-C_3N_4, TEOS-SiO_2/g-C_3N_4, and FA-SiO_2/g-C_3N_4 are 1.34, 1.51, and 1.64 eV, respectively. The variations in the TEOS-SiO_2/g-C_3N_4 and FA-SiO_2/g-C_3N_4 valence band potentials could be attributed to the interaction between SiO_2 and g-C_3N_4. It makes the electron-cloud density of the N atom of g-C_3N_4 in TEOS-SiO_2/g-C_3N_4 and FA-SiO_2/g-C_3N_4 decrease (Fig. 11c), which causes the valence band potential to change due to the variation of the local electric field. In addition, based on the equation $E_{CB}=E_{VB}-E_g$, the conduction band potentials E_{CB} of g-C_3N_4, TEOS-SiO_2/g-C_3N_4, and FA-SiO_2/g-C_3N_4 were obtained as −1.47, −1.32, and −1.14 eV, respectively. The energy-level structures of the three photocatalysts are shown in Fig. 11d. It is evident that the valence band of FA-SiO_2/g-C_3N_4 is positioned more positively, suggesting that its oxidation capability upon photoexcitation is stronger compared to that of g-C_3N_4 or TEOS-SiO_2/g-C_3N_4. This enhanced oxidation potential is advantageous for the catalytic degradation of MB, as it facilitates more efficient electron transfer and oxidation reactions (Zhang et al., 2020).

The electron transfer between FA-SiO_2 and g-C_3N_4 was important for photocatalytic activity. The transient photocurrent density responses are shown in Fig. 12a. The FA-SiO_2/g-C_3N_4 had the strongest light response.

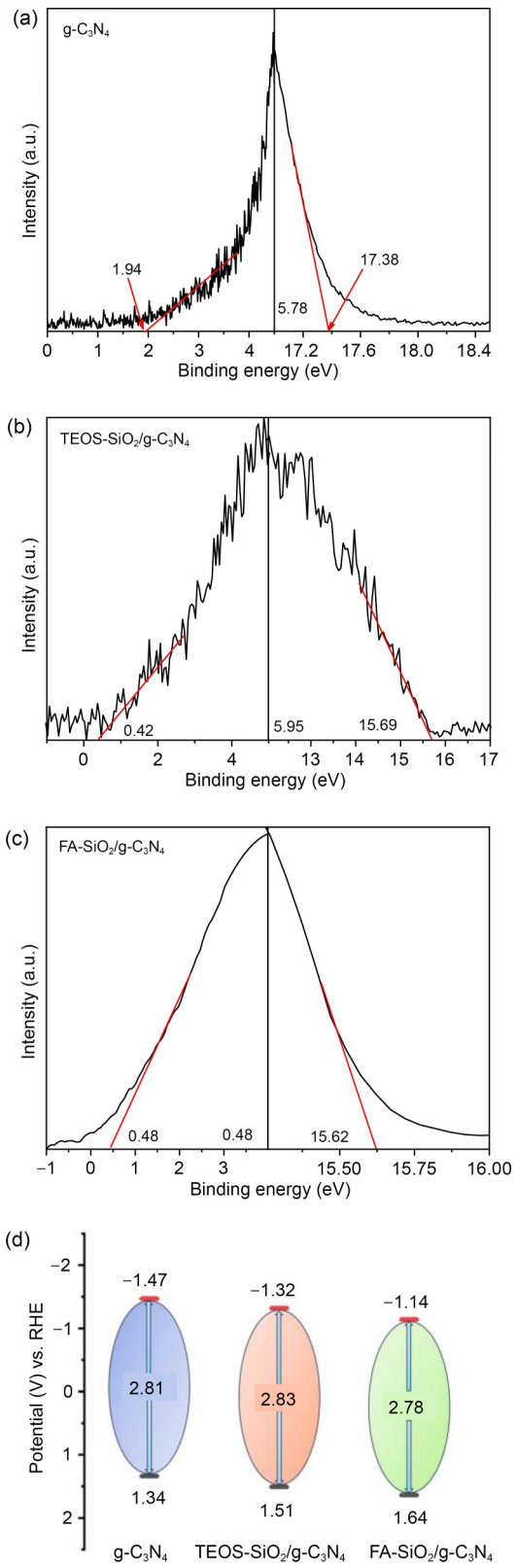

Fig. 11 Ultraviolet photoelectron spectra of (a) g-C_3N_4, (b) TEOS-SiO_2/g-C_3N_4, and (c) FA-SiO_2/g-C_3N_4; (d) energy-level structure diagram

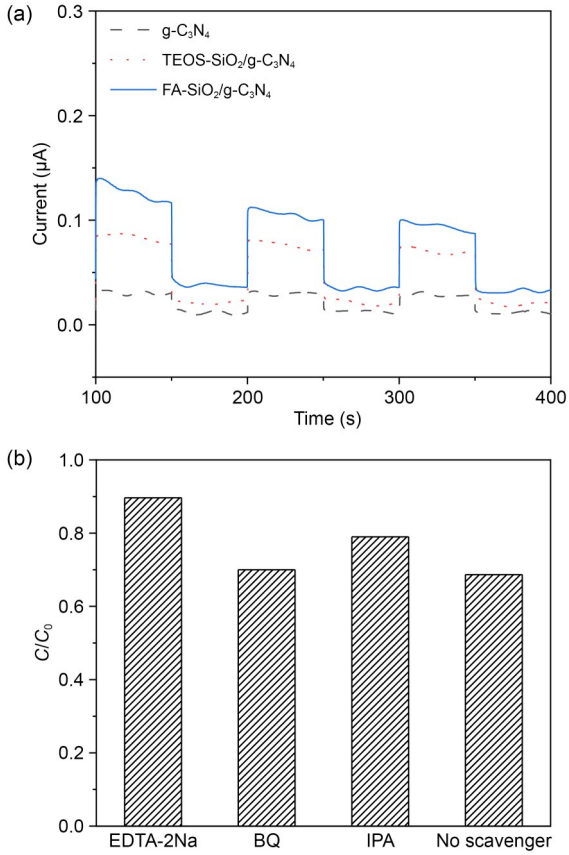

Fig. 12 (a) Transient photocurrent density responses of g-C_3N_4, TEOS-SiO_2/g-C_3N_4, and FA-SiO_2/g-C_3N_4; (b) MB photocatalytic degradation rates of FA-SiO_2/g-C_3N_4 after adding different free radical quenchers

This may be due to the chemical bonding between SiO_2 and g-C_3N_4, which can effectively transfer the electrons between the two materials.

To investigate the active free radicals during photocatalysis, we used ethylenediaminetetraacetic acid disodium salt (EDTA-2Na), benzoquinone (BQ), and isopropanol (IPA) as quenchers for holes (h^+), superoxide radicals ($\cdot O^{2-}$), and hydroxyl radicals (·OH), respectively. From Fig. 12b, one can see that h^+, $\cdot O^{2-}$, and ·OH all participate in the catalytic degradation of MB. A comparison of the degradation rates shows that h^+ dominates the catalytic reaction process.

4 Conclusions

In this study, mesoporous FA-SiO_2 and spherical TEOS-SiO_2 were prepared to modulate the polymerization process of g-C_3N_4. The results show that both the mesoporous structure of FA-SiO_2 and the stacking

pore structure of TEOS-SiO_2 improve the chemical structure of g-C_3N_4. FA-SiO_2/g-C_3N_4 forms a multilevel structure that combines blocks and rods because of the limiting effect of the mesoporous structure of FA-SiO_2, which improves visible-light utilization. We investigated the non-isothermal pyrolysis kinetics of different precursors in an N_2 atmosphere by the TG-DTG method. The mesoporous structure of FA-SiO_2 allows the polymerization reaction of DCDA to occur in a smaller space, which is more favorable for the conversion of DCDA to g-C_3N_4. Photocatalytic experiments showed that the photocatalytic activity of TEOS-SiO_2/g-C_3N_4 and FA-SiO_2/g-C_3N_4 for MB is 1.53 and 3.56 times higher than that of g-C_3N_4, respectively. Compared with TEOS-SiO_2/g-C_3N_4 and pristine g-C_3N_4, the correction of the valence band of FA-SiO_2/g-C_3N_4 leads to its stronger oxidizing ability and higher visible-light utilization efficiency. All of this leads to FA-SiO_2/g-C_3N_4 exhibiting the strongest photocatalytic ability.

Acknowledgments

This work is supported by the Medical Special Cultivation Project of Anhui University of Science and Technology (Nos. YZ2023H2B013 and YZ2023H2B012), China.

Author contributions

Xianhua LI designed the research. Xianhua LI and Qingbo YU processed the corresponding data. Qingbo YU wrote the first draft of the manuscript. Xianhua LI helped to organize the manuscript. Qingbo YU revised and edited the final version.

Conflict of interest

Xianhua LI and Qingbo YU declare that they have no conflict of interest.

References

Angaru GKR, Pal CA, Lingamdinne LP, et al., 2024. High-performance MnO_2 embedded fly ash zeolite applied for effective mineralization of bisphenol-A and sorption of Congo red: mechanism, real water application, and toxicity assessment. *Chemical Engineering Science*, 286:119700. https://doi.org/10.1016/j.ces.2023.119700

Attri P, Garg P, Sharma P, et al., 2023. Precursor-dependent fabrication of exfoliated graphitic carbon nitride (gCN) for enhanced photocatalytic and antimicrobial activity under visible light irradiation. *Journal of Cleaner Production*, 422:138538. https://doi.org/10.1016/j.jclepro.2023.138538

Bansode AS, More SE, Siddiqui EA, et al., 2017. Effective degradation of organic water pollutants by atmospheric non-thermal plasma torch and analysis of degradation process. *Chemosphere*, 167:396-405. https://doi.org/10.1016/j.chemosphere.2016.09.089

Chen L, Ning SB, Liang RW, et al., 2022. Potassium doped and nitrogen defect modified graphitic carbon nitride for boosted photocatalytic hydrogen production. *International Journal of Hydrogen Energy*, 47(30):14044-14052. https://doi.org/10.1016/j.ijhydene.2022.02.147

Chen W, Liu M, Li XY, et al., 2020. Synthesis of 3D mesoporous g-C_3N_4 for efficient overall water splitting under a Z-scheme photocatalytic system. *Applied Surface Science*, 512:145782. https://doi.org/10.1016/j.apsusc.2020.145782

Du H, Ma L, Liu XY, et al., 2018. A novel mesoporous SiO_2 material with MCM-41 structure from coal gangue: preparation, ethylenediamine modification, and adsorption properties for CO_2 capture. *Energy & Fuels*, 32(4): 5374-5385. https://doi.org/10.1021/acs.energyfuels.8b00318

Gnaser H, Savina MR, Calaway WF, et al., 2005. Photocatalytic degradation of methylene blue on nanocrystalline TiO_2: surface mass spectrometry of reaction intermediates. *International Journal of Mass Spectrometry*, 245(1-3): 61-67. https://doi.org/10.1016/j.ijms.2005.07.003

Han LN, Ren WG, Wang B, et al., 2019. Extraction of SiO_2 and Al_2O_3 from coal gangue activated by supercritical water. *Fuel*, 253:1184-1192. https://doi.org/10.1016/j.fuel.2019.05.118

He DY, Liu CH, Zhang YN, et al., 2024. Efficient water disinfection accelerated by polymerization-degree-controlled graphitic carbon nitride under visible light. *Journal of Environmental Chemical Engineering*, 12(2):112247. https://doi.org/10.1016/j.jece.2024.112247

Huang Y, Lin GZ, Hua Z, et al., 2024. Effects of thermal program on physicochemical properties and photocatalytic activity of g-C_3N_4 prepared by dicyandiamide pyrolysis. *Diamond and Related Materials*, 141:110614. https://doi.org/10.1016/j.diamond.2023.110614

Jia YM, Shi ZX, Wang J, et al., 2023. Preparation of Tm^{3+} ion-doped $BaZrO_3$ powder and its luminescence performance study. *Chemical Physics Letters*, 817:140411. https://doi.org/10.1016/j.cplett.2023.140411

Kantor Z, Wu TT, Zeng ZH, et al., 2022. Heterogeneous silica-polyimide aerogel-in-aerogel nanocomposites. *Chemical Engineering Journal*, 443:136401. https://doi.org/10.1016/j.cej.2022.136401

Khan S, Noor T, Iqbal N, et al., 2023. A zeolitic imidazolate framework (ZIF-67) and graphitic carbon nitride (g-C_3N_4) composite based efficient electrocatalyst for overall water-splitting reaction. *RSC Advances*, 13(36):24973-24987. https://doi.org/10.1039/D3RA04783K

Kumar N, Kumari M, Ismael M, et al., 2023. Graphitic carbon nitride (g-C_3N_4)-assisted materials for the detection and remediation of hazardous gases and VOCs. *Environmental Research*, 231:116149. https://doi.org/10.1016/j.envres.2023.116149

Lan ZA, Zhang GG, Wang XC, 2016. A facile synthesis of Br-modified g-C_3N_4 semiconductors for photoredox water

splitting. *Applied Catalysis B: Environmental*, 192:116-125. https://doi.org/10.1016/j.apcatb.2016.03.062

Li JC, Wang C, Ma YX, et al., 2023. In situ formation of red/black phosphorus-modified SiO_2@g-C_3N_4 multi-heterojunction for the enhanced photocatalytic degradation of organic contaminants. *RSC Advances*, 13(19):13142-13155. https://doi.org/10.1039/D3RA01850D

Liu S, Chen XT, Ai WD, et al., 2019. A new method to prepare mesoporous silica from coal gasification fine slag and its application in methylene blue adsorption. *Journal of Cleaner Production*, 212:1062-1071. https://doi.org/10.1016/j.jclepro.2018.12.060

Meng FP, Wang J, Tian WJ, et al., 2022. Graphitic carbon nitride nanosheets via acid pretreatments for promoted photocatalysis toward degradation of organic pollutants. *Journal of Colloid and Interface Science*, 608:1334-1347. https://doi.org/10.1016/j.jcis.2021.10.118

Momin ZH, Lingamdinne LP, Kulkarni R, et al., 2024a. Exploring recyclable alginate-enhanced GCN-LDO sponge for U(VI) and Cd(II) removal: insights from batch and column studies. *Journal of Hazardous Materials*, 469:134015. https://doi.org/10.1016/j.jhazmat.2024.134015

Momin ZH, Lingamdinne LP, Kulkarni R, et al., 2024b. Redefining water purification: gC_3N_4-CLDH's electrochemical SMX eradication. *Chemosphere*, 362:142921. https://doi.org/10.1016/j.chemosphere.2024.142921

Nair KM, Aruchamy G, Thangavelu S, 2024. Zn(II)-MOFs nanosheets interaction with P-doped graphitic carbon nitride nanosheets for effective overall water splitting in alkaline medium. *Journal of Electroanalytical Chemistry*, 952:117968. https://doi.org/10.1016/j.jelechem.2023.117968

Niu WH, Marcus K, Zhou L, et al., 2018. Enhancing electron transfer and electrocatalytic activity on crystalline carbon-conjugated g-C_3N_4. *ACS Catalysis*, 8(3):1926-1931. https://doi.org/10.1021/acscatal.8b00026

Sun WH, Zhu JF, Zheng YH, 2021. Graphitic carbon nitride heterojunction photocatalysts for solar hydrogen production. *International Journal of Hydrogen Energy*, 46(75): 37242-37267. https://doi.org/10.1016/j.ijhydene.2021.09.019

Wan W, Sun JY, Ye S, et al., 2018. Confining the polymerization degree of graphitic carbon nitride in porous zeolite-Y and its luminescence. *RSC Advances*, 8(44):25057-25064. https://doi.org/10.1039/C8RA04436H

Wang N, Cheng L, Liao YL, et al., 2023. Effect of functional group modifications on the photocatalytic performance of g-C_3N_4. *Small*, 19(27):2300109. https://doi.org/10.1002/smll.202300109

Wang TR, Wan T, He SS, et al., 2023. Facile fabrication of graphitic carbon nitride by solvothermal method with hierarchical structure and high visible light photocatalytic activity. *Journal of the Taiwan Institute of Chemical Engineers*, 145:104773. https://doi.org/10.1016/j.jtice.2023.104773

Wang W, Fang JJ, Chen H, et al., 2019. Rice-husk-derived mesoporous 0D/2D C_3N_4 isotype heterojunction with improved quantum effect for photodegradation of tetracycline antibiotics. *Ceramics International*, 45(2):2234-2240. https://doi.org/10.1016/j.ceramint.2018.10.136

Wang WJ, Xu P, Chen M, et al., 2018. Alkali metal-assisted synthesis of graphite carbon nitride with tunable bandgap for enhanced visible-light-driven photocatalytic performance. *ACS Sustainable Chemistry & Engineering*, 6(11):15503-15516. https://doi.org/10.1021/acssuschemeng.8b03965

Weng B, Lu KQ, Tang ZC, et al., 2018. Stabilizing ultrasmall Au clusters for enhanced photoredox catalysis. *Nature Communications*, 9(1):1543. https://doi.org/10.1038/s41467-018-04020-2

Yan SC, Li ZS, Zou ZG, 2009. Photodegradation performance of g-C_3N_4 fabricated by directly heating melamine. *Langmuir*, 25(17):10397-10401. https://doi.org/10.1021/la900923z

Yang XH, Bian XB, Yu WL, et al., 2022. Organosilica-assisted superhydrophilic oxygen doped graphitic carbon nitride for improved photocatalytic H_2 evolution. *International Journal of Hydrogen Energy*, 47(81):34444-34454. https://doi.org/10.1016/j.ijhydene.2022.08.026

Yu ZH, Guan C, Yue XY, et al., 2023. Infiltration of C-ring into crystalline carbon nitride S-scheme homojunction for photocatalytic hydrogen evolution. *Chinese Journal of Catalysis*, 50:361-371. https://doi.org/10.1016/S1872-2067(23)64448-1

Yuan YW, Zhang LL, Xing J, et al., 2015. High-yield synthesis and optical properties of g-C_3N_4. *Nanoscale*, 7(29): 12343-12350. https://doi.org/10.1039/C5NR02905H

Zhang D, Tan GQ, Wang M, et al., 2020. The modulation of g-C_3N_4 energy band structure by excitons capture and dissociation. *Materials Research Bulletin*, 122:110685. https://doi.org/10.1016/j.materresbull.2019.110685

Zhang YZ, Zong SC, Cheng C, et al., 2018. Rapid high-temperature treatment on graphitic carbon nitride for excellent photocatalytic H_2-evolution performance. *Applied Catalysis B: Environmental*, 233:80-87. https://doi.org/10.1016/j.apcatb.2018.03.104

Zhao QH, Fu LJ, Jiang DH, et al., 2018. A nanoclay-induced defective g-C_3N_4 photocatalyst for highly efficient catalytic reactions. *Chemical Communications*, 54(59):8249-8252. https://doi.org/10.1039/C8CC04100H

Electronic supplementary materials

Table S1, Figs. S1–S7